The Electrochemical Society
Advancing solid state & electrochemical science & technology

Towards Long-Term Monitoring of Commercial Lithium-Ion Batteries Enabled by Externally Affixed Fiber Sensors and Strain-Based Prognostic Strategies

View the article online for updates and enhancements.

Towards Long-Term Monitoring of Commercial Lithium-Ion Batteries Enabled by Externally Affixed Fiber Sensors and Strain-Based Prognostic Strategies

Sasan Ghashghaie,[1,2,z] Julien Bonefacino,[3] Yin-Nee Cheung,[1] Xin Cheng,[2] Mingde Wang,[4] Hwa-Yaw Tam,[2] Jean-Marie Tarascon,[3] and Steven T. Boles[1,5,*,z]

[1]*Centre for Advances in Reliability and Safety, New Territories, Hong Kong, People's Republic of China*
[2]*Department of Electrical and Electronic Engineering, The Hong Kong Polytechnic University, Kowloon, Hong Kong, People's Republic of China*
[3]*Collège de France, Chimie du Solide et de l'Energie—UMR 8260 CNRS, Paris, France*
[4]*GP Technology & Innovation Limited, 7/F, 16W, Hong Kong Science Park, Hong Kong, People's Republic of China*
[5]*Department of Energy and Process Engineering, Faculty of Engineering, Norwegian University of Science and Technology (NTNU), Trondheim, Norway*

Real-time monitoring of both continuous and spontaneous degradation in lithium-ion batteries is challenging due to the limited number of quantitative metrics available during cycling. In this regard, improved sensing approaches enabled by sensors of high accuracy, precision, and durability are key to achieving comprehensive state estimation and meeting rigorous safety standards. In this work, external temperature and strain monitoring in commercial Li-ion button cells was carried out using tandem pairs of polymer-based and silica-based optical fiber Bragg grating sensors. The decoupled data revealed that the sensors can reliably track strain and temperature evolution for over 500 cycles, as evidenced by periodic patterns with no sign of sensor degradation or loss of fidelity. Moreover, monitoring the strain signal enabled early detection of an anomalous cell over ∼60 cycles ahead of an electrochemical signature and abrupt drop in capacity, suggesting that mechanical sensing data may offer unique benefits in some cases. Detailed mechanical monitoring via incremental strain analysis suggests a parallel path toward understanding cell degradation mechanisms, regardless of whether they are continuous or discrete in nature. The accuracy and durability of such a package-level optical fiber sensing platform offers a promising pathway for developing robust real-time battery health monitoring techniques and prognostic strategies.

Despite the rapid growth of Li-ion battery (LIB) technology over the last two decades, the development of LIBs has been surprisingly conservative (particularly with respect to the implementation of new materials and production methods), owing to both the need for extreme reliability during regular usage, as well as rightful concerns about cell malfunctioning (stemming from electrical, thermal, or mechanical anomalies, sometimes leading to catastrophic swelling or thermal runaway).[1–3] From this standpoint, precision assessment of battery reliability and safety at the earliest stages can increase the pace of development and improve sustainability. To this end, real-time monitoring of a cell's dynamic thermal, chemical, and mechanical condition during cycling can enable such precision assessment, provided that sampling rates and accuracy are sufficient for the respective failure or degradation mode. Thus, it becomes clear that reliable long-term observation of critical cell parameters involved in the aging process will lay the basis for more accurate health assessments, enabling effective fault diagnosis and degradation diagnostics.[4]

Challengingly, long-term tracking of the cell state has been inhibited by the limited number of observables during cycling. While conventional electrochemical parameters such as capacity, voltage, and impedance are essential for monitoring a cell's general state,[5–7] gaining a deeper insight into the various primary and parasitic reactions at different stages of charge and discharge may require another level of diagnostic sensing: Ideally, direct physio-chemical probing of molecules and ions can be deployed to quantify the dynamic electrochemical environment inside a cell, as has been shown recently with IR-FEWS.[8] However, given the various challenges associated with this method, measurement of thermodynamic parameters, including temperature, strain, and pressure (T, ε, P) [4], may be sufficient for improved quantitative monitoring of a cell over time.

Regardless of whether the tracking of thermo-mechanical parameters (T, ε, P) is conducted inside a cell or externally on the surface of a cell, each case necessitates using sensors of high precision and sufficient durability to ensure optimal cell evaluation.[9] Since LIBs are sealed systems, external measurement strategies should have an advantage over internal pressure sensing approaches as they eliminate the need for (and risks from) casing modification. Package-level measurements can be used to monitor temperature changes[10] and the volumetric changes of the cell due to regular (de)intercalation of Li-ions (from)into the electrodes or the irreversible expansion-inducing effects, such as gas build-up,[11,12] the growth of solid-electrolyte interface (SEI) film,[13] and Li-plating on the anode surface.[14–16] Importantly, methods that rely on outputs such as terminal voltages and cell capacity [17] may fail to identify anomalous behavior at the earliest stages; hence, alternative quantitative metrics like cell expansion [18] and localized temperature changes may telegraph cell behavior in ways that are currently unrealized and unutilized.

Different methods have been employed to measure package expansion including strain gauges,[17,18] dilatometry,[19] piezo-sensors,[20] optical reflection-based,[21,22] etc. In recent years, fiber Bragg grating (FBG) optical fiber sensors have been employed in electrochemical energy storage systems such as fuel cells[23,24] and Li(Na)-ion batteries[8,25] for real-time monitoring of temperature, strain, and pressure. Regarding their fast response, low cost, light weight, scalability, and selective sensing capability, the convergence of fiber optic strategies with various Li-ion battery configurations might be transformative in the industry as a reliable observation solution enabling outputting of data for multiple parameters in real time, simultaneously.[26] Since the first report by G. Yang et al.[27] on the

*Electrochemical Society Member.
zE-mail: sasan.ghashghaie@polyu.edu.hk; steven.boles@ntnu.no

application of FBG sensors for real-time temperature measurement in Li-ion batteries, multiple studies have been conducted on operando observation of temperature, strain, and pressure in various Li-ion platforms[4,28–32] with clear prioritization towards feature extraction from individual charge/discharge or short term cycling.

Although these studies clearly demonstrate various capabilities of optical fiber sensors to monitor key cell parameters during electrochemical cycling, there is still a research gap concerning the durability and reliability of the output optical data during extended cycling up to several hundreds of cycles. We recently demonstrated the application of the Bragg grating polymeric optical fibers (POF) for high-fidelity observation of temperature and strain at the package level for Li-ion cells during galvanostatic cycling.[33] In the present study, the same non-invasive optical sensing platform, including tandem pairs of POF and silica-based single-mode (SMF) FBGs, both affixed on the external surface of the cell, is employed to monitor the device-level volume change and thermal events in commercial Li-ion button cells for over 500 cycles. Although numerous ways exist to interpret and extract value from the strain signal, we show that the simple amplitude (difference between maximum and minimum values in a cycle) may be one possible health indicator for advance detection of anomaly long before a serious failure. As a complementary approach, we show that further consideration of secondary data through differential strain analysis may offer excellent correlations with capacity slippage and open new possibilities for alternative health indicators in battery management systems and prognostic methods. Interestingly, data harvested from multiple cells initially tagged as "faulty" by the manufacturer showed that a significant number of them were otherwise indistinguishable from healthy cells over long-term cycling. These results underscore the imprecise nature of validation by manufacturers, justifying new protocols for improving yields and lessening false negative and false positive ambiguity.

Experimental

Cell chemistry and electrochemical measurements.—1258 button cells of two different types were provided by GP Batteries Ltd (GP) for testing. As specified in Table I, the two types had identical cathodes made of $LiCoO_2$ (LCO) but different anode compositions. The anode of the first type (G) is made of graphite, with a rated cell capacity of 60 mAh. The second type of battery (SC) is composed of a blended $SiOx/C$ anode (approximate silicon content of over 10%) with a rated cell capacity of 70 mAh. Regarding the exclusiveness of electrolyte formulation, it is only disclosed to be a commonly used electrolyte in rechargeable Li-ion batteries comprising $LiPF_6$ dissolved in carbonate-based solvents. The GP cells have jelly-roll configuration and were received as-fabricated just prior to the SEI formation process. After the SEI formation was accomplished according to the protocol prescribed by the manufacturer, the cells were run at 0.5 C/0.5 C until they reached the failure threshold defined as 80% of the initial capacity. The investigation of the formation cycles is not explicitly envisioned for this study, but nevertheless, sensor data from these cycles is provided in the Supplementary Information for context (Fig. S2). The protocols for normal cycling of the graphite anode (G1/G2) and $SiOx/C$-anode (SC) cells, as provided by the manufacturer, are listed in Table II. The electrochemical cycling tests were conducted in a climate chamber (Vötsch Industrietechnik) at a constant temperature of 25 °C using a LANHE CT3002A battery testing system. The authors take the opportunity to note that although three cells are

reported herein, over ten cells were tested in a broader study in collaboration with GP Batteries Ltd (discussed later). While SC and G1 are reported based on their "typical" cycling characteristics and differing anode chemistries, G2 was indeed an anomaly and thus complements the reference case provided by G1.

Sensor design and sensing methodology.—In our experiments, two types of optical fibers, including a commercial silica single-mode fiber (Silitec G657.B germanium doped fiber) and a polymer optical fiber (POF) made of Zeonex, were used. Polymer fibers are known to have enhanced environmental sensitivities compared to their silica counterparts due to their low Young modulus.[34] More information about the fabrication of polymer fibers can be found elsewhere.[35] The optical sensors employed in this study consist of 3-mm FBGs inscribed within the core of both silica and POF using the phase-mask method with an excimer laser at 248 nm (Braggstar M, Coherent Inc., Santa Clara, CA, USA).

The thermal sensitivities of the fabricated FBGs are 9.62 pm/°C and −22.09 pm/°C for SMF and POF fibers, respectively, giving POF a thermal response two times larger than that of the SMF fiber. POF also showcases a higher strain sensitivity of 1.52 pm/$\mu\varepsilon$ versus 0.839 pm/$\mu\varepsilon$ for SMF.[33] These significant differences in the temperature and strain sensitivities enable the decoding of strain and temperature events using the algorithm referenced by Huang et al.[4] The FBGs signals were recorded using the optical interrogator Luna Innovations (Si155).

To hold the cell in a fixed position while giving it sufficient room for expansion, 3D cell holders were designed using Solidworks and 3D-printed by ANYCUBIC I3-Mega. The negative and positive terminals of the accommodated cell were connected to the battery tester using copper strips and conductive silver paste to avoid the risk of clamping pressure from the electrical contacts. It was demonstrated in our previous study[33] that such methodology did not impair the normal cycling of the batteries while allowing for reliable temperature and strain measurements.

After securing the cell inside the mould hole, SMF and POF were placed close to each other on the negative-terminal side of the package surface and glued using a commercial twin epoxy (Araldite fast-setting epoxy adhesive), which was left to cure overnight. To facilitate heat transfer during cycling, the thermal paste (STARS-612, Balance Stars) was applied prior to positioning the fibers on the surface. During the affixing process, the fibers are slightly pre-strained, and once fibers are fixed, thermal expansion at the package level will generate tensile strain in the sensors. Therefore, the thermal sensitivity of both SMF and POF changes once the epoxy is completely cured,[15] and the glued sensors must be thermally calibrated before electrochemical cycling. A schematic view representing the button cell's fixture along with the copper foil extension and the FBG sensors affixed on the surface of the package is shown in Fig. S1a. The complete experimental set-up is shown in Fig. S1b. Thermal calibration was carried out between 25 °C to 33 °C to avoid affecting the electrolyte. It's worth mentioning that silica-based FBGs and Zeonex-based FBGs show linear thermal response up to 700 °C[36] and 70 °C,[35] respectively. It should be noted that the strain sensitivity of both SMF and POF was measured before mounting them on the cell and remains unchanged during the cycling. The thermal sensitivities of the glued fibers on all cells are summarized in Table III. It is worth noting that if the fibers could be placed on the cells with the same amount of pre-strain every time, this should allow us to neglect the thermal calibration stage, saving considerable time. With only logical operations remaining, a Python script was written to apply the appropriate mathematical operations to decouple strain and temperature.

Results and Discussion

The comprehensive long-term electrochemical performance of cell SC up to 530 cycles (failure threshold) at 0.5 C/0.5 C is shown in Fig. S3, establishing a general impression of cell-stability, given

Table I. Specifications of the tested Li-ion button cells.

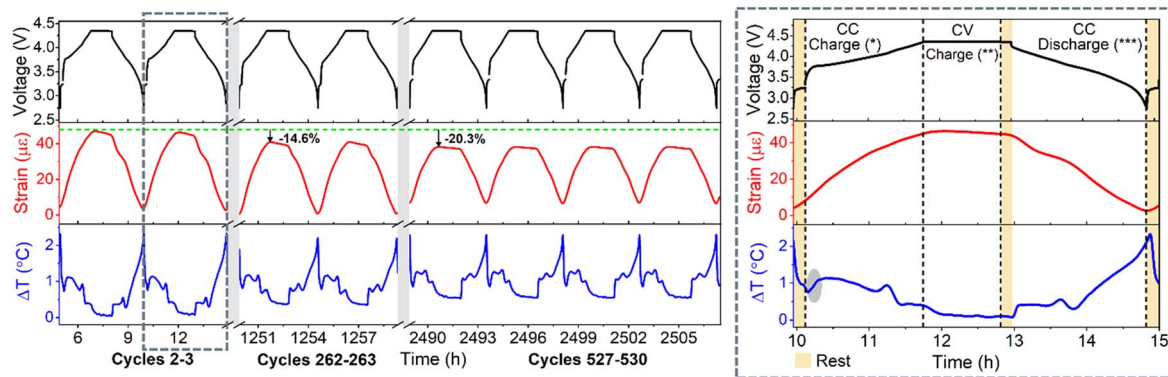| Cell No.	Model Name	Anode Composition
SC	GP1258–07HDS	Graphite + 10% SiO_x
G1	GP1258–06HD	Graphite
G2	GP1258–06HD	Graphite

Figure 1. Decoupled strain and temperature response in conjunction with galvanostatic voltage profile for 530 cycles at 0.5 C/0.5 C for cell SC in different time slots.

Table II. Cycling conditions for SC, G1, and G2 li-ion button cells.

Cell	SC	G1,G2
Anode material	10% SiO$_x$/C	Graphite
Rated capacity (mAh)	70	60
Cycling condition (0.5 C/ 0.5 C)	CC 35 mA to 4.35 V	CC 30 mA to 4.35 V
	CV 4.35 V to 1.4 mA	CV 4.35 V to 3 mA
	rest 10 min	rest 10 min
	followed by	*followed by*
	CC 35 mA to 2.75 V	CC 30 mA to 2.75 V
	rest 10 min	rest 10 min

the lack of anomalies in the capacity-voltage plots and the steady declination seen for cycle number-capacity as it reaches the failure threshold. As is typical for the behavior of Li-ion cells made of SiO$_x$-blended anodes, the profiles include sloping plateaus during charge and discharge.[35]

Durability of FBG sensors over cycling.—The decoupled strain and temperature values of SC in conjunction with the voltage profile for three intervals are presented in Fig. 1 for clarity, with the full-time series shown in Fig. S4 (where the green highlight denotes the regions illustrated in Fig. 1). It is clearly seen that FBG sensors track the periodic evolution of strain and temperature on the external package surface in a reversible and repeatable manner, including numerous characteristic peaks and slopes. Regarding the mechanically driven expansion, the sensor undergoes tensile straining and increases continuously, stemming from the volumetric expansion at the cell level, as seen in Fig. 1 (right, region *, and also demonstrated in[13]). Naturally, the cell volume decreases as the anode contracts during the following discharge step (Fig. 1, right, region ***), leading to the observed reversible "strain" behavior for each cycle.

Bridging to the material level, for the SC cell, a volume change of ~22% may be expected, with 2% coming from LCO's non-intuitive unit cell volume expansion during delithiation[37,38] and a

rough estimation of 20% coming from the full lithiation of a 10% SiO$_x$/90% graphite mixture, (based on a rule of mixtures[37,39]). However, this fails to account for the mechanically critical role of the binder, which may, in turn, reduce the electrode expansion to ~2%-8% depending on mass loading, porosity, etc.[40] How exactly does this material level expansion and contraction propagate to the electrode level and then further to the sensors affixed on the battery surfaces detected here is often considered to be poorly understood.[41]

The repeated thermal evolution of the cell, as evidenced in Fig. 1, clearly shows that whether monitoring during the first 15 h of cycling or nearly 2500 h later, the temperature fluctuations recorded by the sensors are remarkably similar. The overall trend follows a repeatable progression with the discharging of the cell leading to a rapid rise in temperature due to mass transport limitations and corresponding heat release in the cell (Fig. 1, right, region ***).[42] Following a brief rest period, the temperature drops rapidly, and then a minor increase in temperature is noted again when the cell's constant current charging begins (Fig. 1, right, region * and highlighted with the grey ellipse). However, as this step necessitates the delithiation of LCO, the overall change is relatively moderate, and small fluctuations are noted, but generally less than 0.5 °C. During the constant voltage charging stage (Fig. 1, right, region **), the temperature relaxes and resolves to a local minimum, after which discharging begins and the process repeats. Clearly noted here in Fig. 1 (and Fig. S3) is the gradually increasing base temperature of the cell. With a steadily growing overpotential in the cell (discussed later in the text), a continuous heat-generating situation may arise, though a more appropriate determination of heat contributions from entropy, enthalpy, and loss is needed to explore the different sources.[42–44]

To understand the consistency of strain and temperature monitoring during the initial three charge-discharge cycles compared to the final three cycles, the thermo-mechanical readings for SC and G1 are plotted in Figs. 2a and 2c, respectively. Despite substantial reductions of 17%-70% in magnitude, the features that appear on the strain profiles during the initial cycles are roughly observed in the last cycles regardless of cell chemistry. On the other hand, temperature profiles show a consistent temperature drop of ~1.5 °C during the rest step between charging and discharging, regardless of age. However, the magnitude of the temperature fluctuations within each cycle clearly diminishes as the cell ages, regardless of chemistry. The consistency between electrochemical aging and the

Table III. Thermal sensitivities recorded during the calibration of the investigated cells.

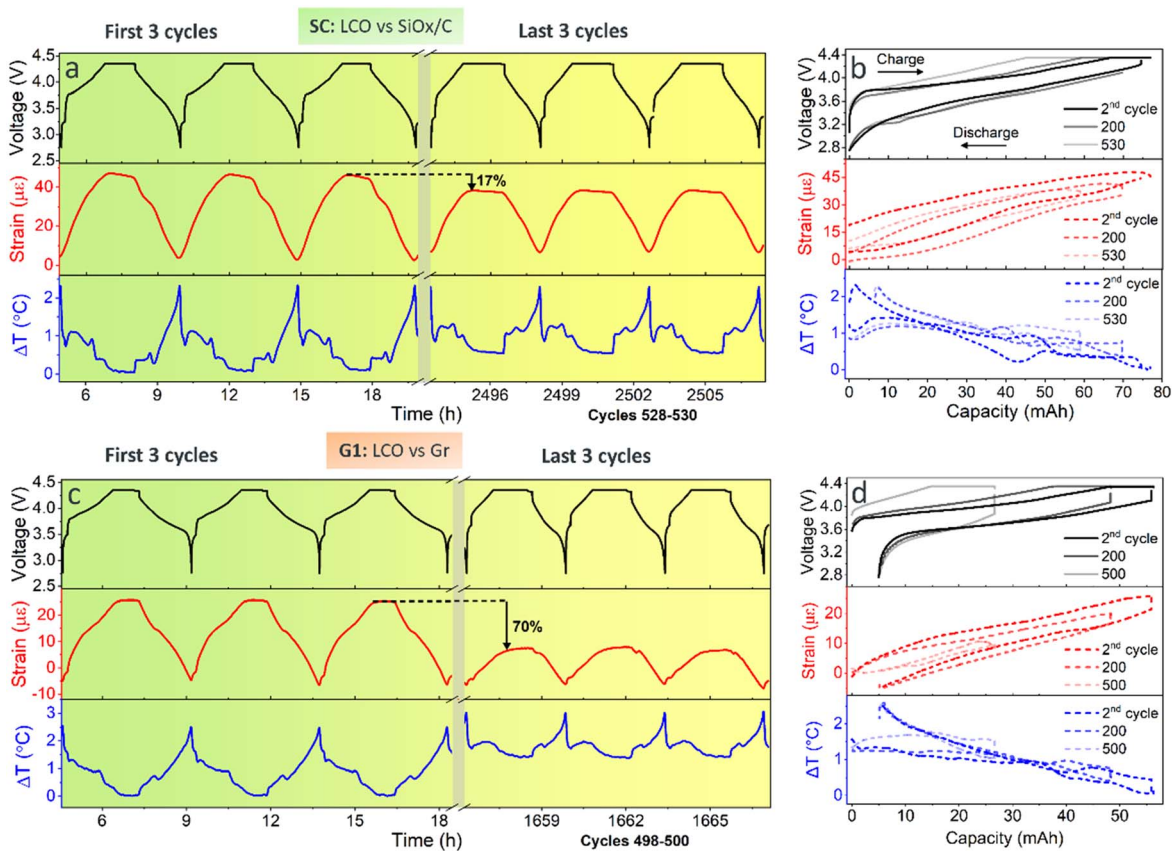|	Thermal sensitivity of glued SMF (pm/°C)	Thermal sensitivity of glued POF (pm/°C)
Graphite anode cell (G1)	11.47	−41.40
Graphite anode cell (G2)	11.85	−79.32
SiO$_x$/C anode cell (SC)	11.42	−30.85

Figure 2. Voltage profile along with the strain and temperature response during the first three and last ten cycles of SC (a) and G1 (b). Capacity vs voltage, strain, and temperature for SC and G1, respectively, are shared in (b) and (d) indicating the decay of all three parameters as the cells age.

thermo-mechanical status of the cell is clearly demonstrated in Figs. 2b and 2d, where the strain and temperature loops diminish over cycle aging regardless of the chemistry.

Considering cell G1 further, Fig. S5 shows the electrochemical cycling results at 0.5 C/0.5 C for 500 cycles. Although the cell reached the failure threshold after 275 cycles, cell monitoring was continuously carried out for up to 500 cycles to track strain and temperature over a sufficiently lengthy span. The decoupled strain and temperature, in conjunction with the voltage profile for G1, are shown in Figs. S6, and S7 demonstrates the periodic pattern of the decoupled strain and temperature at different time slots, as high-lighted in Fig. S6. Considering the temperature profile in Fig. S6, the increase in the cell average temperature is attributed to the continuously increasing overpotential and decreasing thermal conductivity[45] as the cell ages. Also, Fig. 2c reveals that the FBG sensors reproducibly track the evolution of strain and temperature during consecutive charge-discharge cycles. Similar to cell SC, the erosion of the strain peaks, along with the drop in the intensity of the temperature features, is indicative of cell degradation during electrochemical cycling.

Strain amplitude as a primary health indicator.—Given the striking trend of decreasing magnitude of strain with each cycle oscillation (regardless of cell type), a simple vector to scalar reduction becomes both justified and interesting. As such, strain amplitude is again considered a health indicator, as suggested previously.[33] The correlation between the strain amplitude and capacity up to over 500 cycles is quantified in Figs. 3a and 3c for SC and G1, respectively. For cell SC (Fig. 3a), the strain amplitude is nicely correlated to the capacity fading of the cell over more than 500 cycles. Concerning cell G1 (Fig. 3c), the consistent trends between state of health and strain amplitude carry on even after the technical failure threshold (275 cycles), suggesting a robustness of

the strain signal in response to the internal cell events. Figure 3c also shows that as different degradation mechanisms are likely triggered during cycle aging, the slope of the capacity fading trajectory also changes, which is nicely evidenced by observing the strain ampli-tude (Dashed line arrows on Fig. 3C).

To quantify the correlation more explicitly, we employ a strain-based state-of-health SoHε index[33]:

$$SoH_\varepsilon(\%) = \frac{Actual \quad discharge \quad strain \quad amplitude}{Initial \quad discharge \quad strain \quad amplitude} \times 100$$

Figures 3b and 3d show that a linear correlation exists between the SoHε and that achieved by discharge capacity (SoH_Q) for SC and G1 cells, respectively, further supporting our observation that the evolution of package-level strain amplitude can be a measure of the cell state in Li-ion batteries. Interestingly, the slope of the linear fit is close to unity for SC, which means the SoH estimated using the strain amplitude in SC for a given cycle matches that obtained by the discharge capacity. We note that this estimation utilizes hundreds of data points needed for the long-term fitting and that with shorter SoH intervals, such correlations may not be so clear. While promising, further studies with more stochastic charging protocols and rest periods are warranted to determine the viability of strain amplitude as a primary health indicator in different types of lithium-ion batteries.

Early warning signaling to spot anomalous behavior.—The second graphite-anode cell tested in this study is cell G2. Although G1 and G2 were nominally identical cells in terms of the chemistry, manufacturing parameters, and formation process, the electrochemical results shown by Fig. S8a and S8b reveal that G2 experiences a significant capacity drop after 89 cycles followed by sharp spikes appearing on the voltage profile from the 90th cycle onwards.
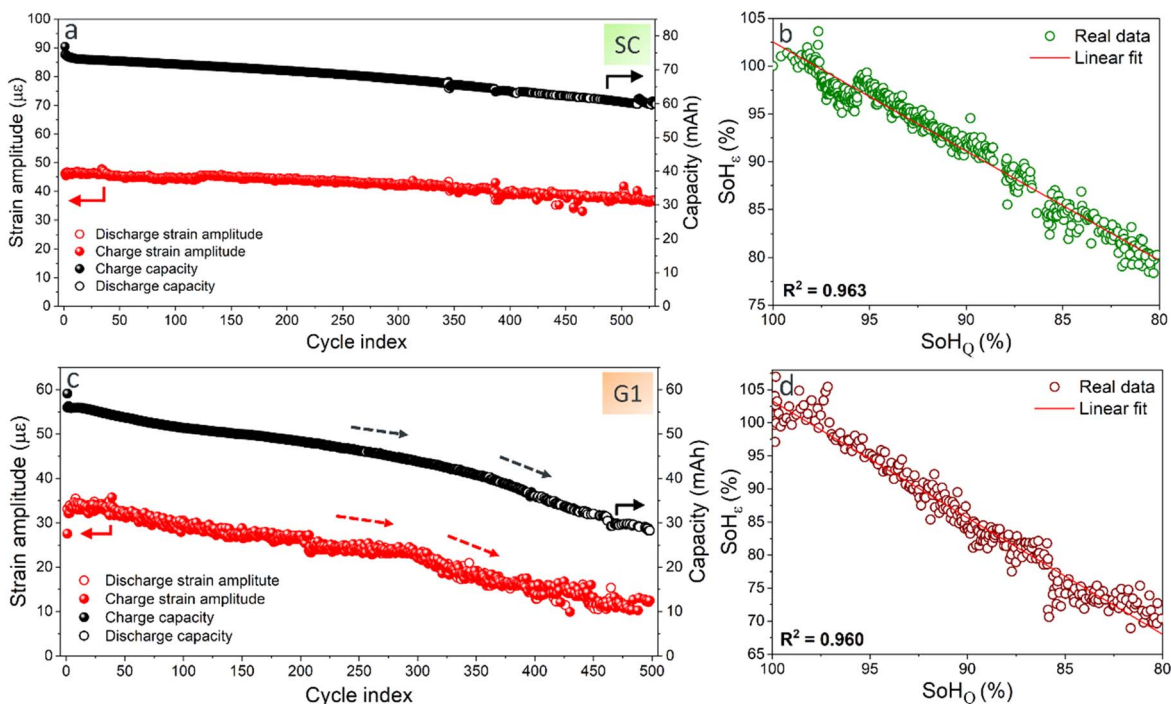
Figure 3. The evolution of strain amplitude during cycle aging at 0.5 C/0.5 C in cell SC (a) and G1 (c). The linear correlation between the SoH values obtained by capacity and strain amplitude in SC (b) and G1 (d).

Figure S8c shows that the cell undergoes a sudden death as a critical point occurs after 89 cycles, whereby an abrupt shift in the degradation mechanism appears to take hold, and the predictability of the cell disappears. As a result of this failure, the capacity drops by around 30% just two cycles after the electrochemical anomalies appeared.

The decoupled data in Fig. 4a shows significant disruption of strain and temperature after ∼90 cycles/400 h, which is concurrent with the emergence of the irregular voltage signal. However, the more important observation here may be that the strain signal displays a certain degree of spontaneous inflation/deflation during the intermediate cycles long before the cell reaches sudden death. This is more evidently shown in Fig. 4b, where the amplitude of the strain profile is larger after 175 h (56 $\mu\varepsilon$) (highlighted in yellow) than both after 52 h (38 $\mu\varepsilon$) and 350 h (35 $\mu\varepsilon$). A comparison between the strain amplitude evolution and capacity, as shown by Fig. 4c, reveals that the strain amplitude during charge and discharge undergoes a 50% rise from 40 $\mu\varepsilon$ to nearly 60 $\mu\varepsilon$ between the 25th and the 30th cycle. In contrast, the output capacity remains stable throughout the entire cycling span until the critical point reached the 89th cycle.

The substantial rise and fall of strain amplitude while the capacity follows a smooth fading trajectory goes against our observations of cell SC and G1 (shown with faded red circles in Fig. 4c) where strain amplitude was consistently correlated with capacity. This means that simultaneous with the storage/extraction of Li ions into/from the anode electrode, some phenomena(-on) with a remarkable impact on the volumetric changes of the package are(is) occurring within the cell G2, but with some degree of reversibility or transient nature. Apart from the root internal cause of this abnormal volume change, which is beyond the scope of this study, capturing such a signal by the SMF-POF FBG sensors tandem is highly fortuitous as it suggests an ability for advance warning before the cell electrochemically faces an abrupt failure. In other words, although the data is captured on the package surface, the FBG sensors can spot abnormal mechanical fluctuations inside the cell during cycling, and this anomaly was not apparent from either thermal or electrochemical observables. Also worth considering is that the warning signal appears around 60 cycles (over 200 h) ahead of the critical point,

providing a sufficiently broad prognostic distance to prevent catastrophic failure. This result underscores the relevance of mechanical expansion and contraction in offering a facile fault diagnostic solution for increased battery safety without the need for intricate calculations or computation for onboard situations.

Although the root cause analysis of cell G2 abrupt failure is not within the scope of the present study, the X-ray microscope images of cells G1 and G2 taken before and after cycling (shown in Fig. S9) reveal that while G1 undergoes a slight jelly roll deformation after 500 cycles (marked with the yellow arrow), in G2 the jelly roll is partially covered with black spots (marked with yellow dashed line), which could indicate discrete, localized malfunction within the cell.

As noted in Experimental section, the cells discussed here (i.e., G1, G2, and SC) were part of a more extensive study in cooperation with GP to verify the reproducibility of the methodology. Consequently, a group of the SiO$_x$/C-anode cells (denoted as B.13, B12, B11, B10, B.9, and B.8) were flagged as faulty cells by the manufacturer according to their internal cell validation protocols, and these cells were tested under the same conditions. The evolution of normalized strain amplitude for these cells, along with that of a healthy cell of the same chemistry (SC-ref), is shown in Fig. 5a. Worth noting that the SC-ref and the batch B cells have all had their formation steps completed at the factory. It is clearly seen that SC-ref follows a steady degradation trend between both strain and capacity (Fig. 5b). Interestingly, the "faulty cells" display consistent capacity degradation over time for the first 120 cycles, but their mechanical evolution, vis-à-vis strain amplitude, varies dramatically. Collectively, these results suggest that while internal cell validation protocols may indeed be sufficient to identify "faulty" cells, the risks of false-positive and false-negative screening are by no means perfect science. Our results suggest that by adding further screening metrics, spotting the faulty cells can be carried out more efficiently, mitigating the risk of scrapping healthy cells.

Differential analysis.—In addition to the primary health indicators, such as capacity and strain amplitude, differential analysis can be used to generate secondary features characteristic of the SoH of a Li-ion cell.[46] For this purpose, incremental capacity analysis (ICA)
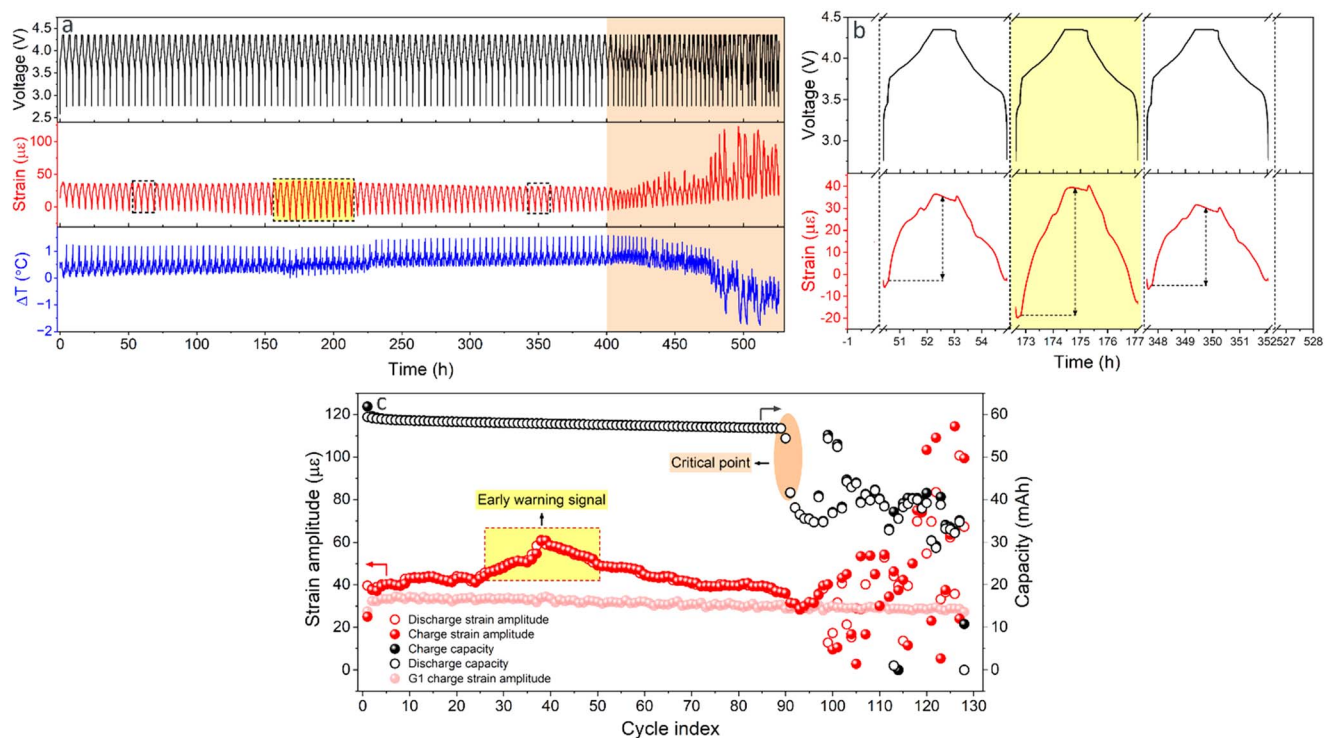
Figure 4. (a) Inflation of strain signal of G2 in the middle of electrochemical cycling at 0.5 C/0.5 C, while the voltage profile is stable. (b) A zoomed-in view of the intervals marked with the dashed line across the strain profile in Fig. 4a. (c) The evolution of strain amplitude during cycle aging at 0.5 C/0.5 C in cell G2 (plain red) in conjunction with capacity variation. A critical failure point is detected after 89 cycles. For comparison, the strain amplitude of cell G1 is also displayed on the graph (shaded red).
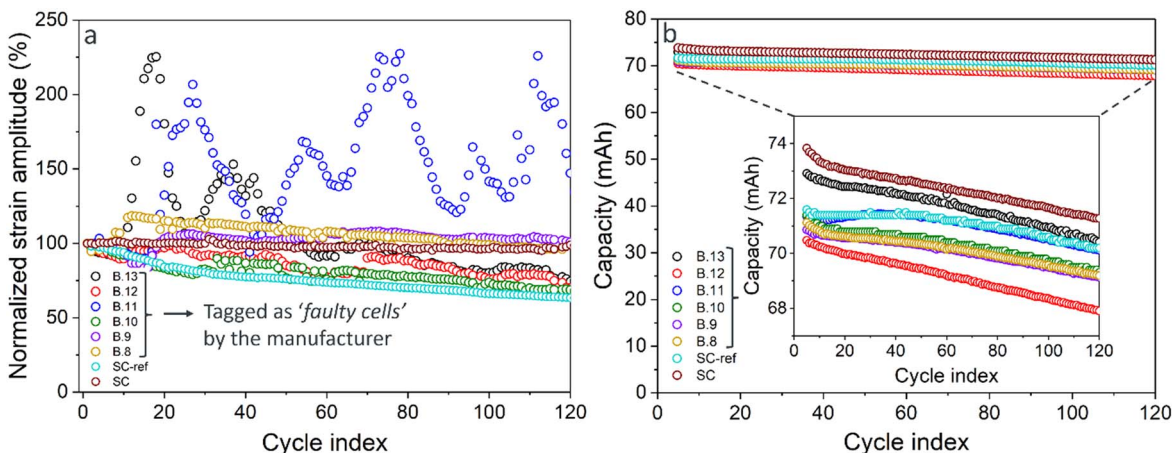

Figure 5. Normalized strain amplitude (a) and capacity evolution (b) for the healthy cells (SC-ref and SC) and cells tagged as faulty (batch B).

has been widely employed as a non-invasive in situ electrochemical technique to estimate the internal cell state and explore degradation mechanisms.[47] The ICA plots are obtained by differentiating the cell capacity over potential (i.e., dQ/dV) during charge or discharge, with the peaks representing the electrochemical reactions and phase transitions. Previously, we demonstrated that the peaks and features of ICA analysis on LFP-LTO coin-cells located at the same potential as those of the incremental strain analysis (ISA), obtained by differentiating the strain over potential (i.e., dε/dV), in the first 16 cycles.[33]

The filtered dQ/dV and dε/dV profiles during charge and discharge at different cycles of SC and G1 are shown in Figs. 6a–6d and 6e–6h, respectively, where it can be seen that the characteristic charge and discharge peaks are concurrent in both dQ/dV and dε/dV for over 500 cycles, indicating the consistency

between the secondary electrochemical and mechanical features during long-term cycling. From the asymmetry of material expansion, the anode is expected to dominate the dε/dV signal, but nevertheless, the similarity between the features is striking, given the difference in their acquisition method.

Herein, the charge dQ/dV peaks with a corresponding positive dε/dV peak (cell expansion, "a" and "a‴" in Figs. 5a and 5c, respectively) are primarily contributed by the formation of Li_xSi alloys upon anode lithiation.[48,49] The Si-based products will then be converted back to amorphous Si upon the delithiation process during discharge ("b"/"c" and "b‴"/c‴" in Figs. 5b and 5d, respectively). In G1 (Figs. 6e–6h), peak "a" represents a structural change from dilute stage-1L to stage-4L, while peak "b" is constituted by the graphite transition from stage-3L to stage-2L along with the LCO hexagonal-I to hexagonal-I/II phase transition.[50,51] The more subtle peaks "c"
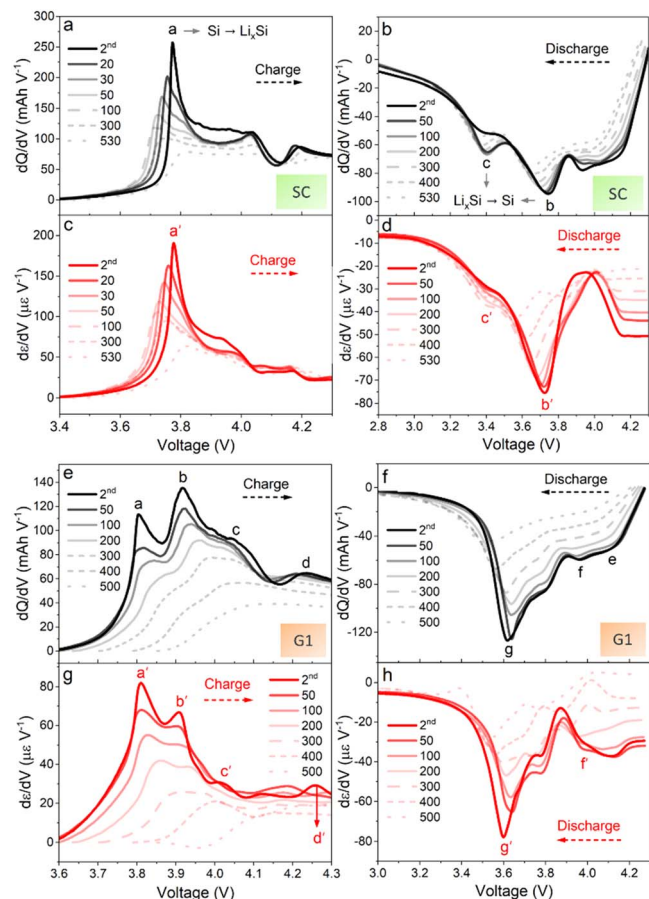
Figure 6. Incremental capacity analysis (ICA) in conjunction with the incremental strain analysis (ISA) for SC (a)–(d) and G1 (e)–(h).

and "d" represent the reversible phase transitions of LCO upon delithiation from hexagonal-I/II to hexagonal-II and hexagonal-II to monoclinic, respectively.[52] Comparing the differential capacity plots to those of differential strain, this analysis strongly supports the attribution of strain changes to those of the anode, while the structural changes of the cathode are better captured by noting that the position of peaks "c" and "d" are coincident with the thermal peaks noted previously in Fig. 1.

Interestingly, a comparison between the differential profiles of G1 and G2 in Fig. S10 reveals that while the charge dQ/dV curves of G1 and G2 possess virtually the same features and intensities, the corresponding dε/dV profile of G2 exhibits much higher intensities for the first two charge peaks along with an extra peak at around 4.1 V. This obvious difference in the dε/dV features suggests one possible strategy for differentiating the healthy cells from the anomalous ones during initial cell testing routines.

Turning to the prospects for long-term tracking, the evolution of quantified dQ/dV peak characteristics such as intensity and position has been widely employed to monitor cell status during cycle aging.[53] In electrochemical terms, the intensity of the dQ/dV peaks is directly proportional to the contribution of the respective reactions to the cell's overall capacity, but this, of course, depends on contributions from the anode and cathode half-cell reactions. An unbalanced loss of active material (anode or cathode) will lead to changes in the peak positions and intensities, commonly referred to as slippage. However, in a half-cell, a peak position change with fixed intensity will indicate an overpotential required for the reaction to occur. From Figs. 7a and 7c, it can be seen that there is a strong consistency between the trajectory of dQ/dV and dε/dV peak intensity and position (using "a" and "a‴" from Figs. 6a and 6c, formation of Li_xSi) over 530 cycles in cell SC. The consistency

between the dQ/dV and dε/dV peak properties for SC is also observed during discharge, as shown by Figs. 7b and 7d (using "b" and "b‴" from Figs. 6b and 6d), where the steady shift of dQ/dV and dε/dV peaks towards lower potentials is consistent with cell aging. As for pinpointing which aging mechanism is responsible for the shifting in dε/dV, further studies are needed to understand how slippage and loss of active material in the cathode would affect the strain evolution of the cell, considering that the anode is the primary contributor to dε/dV peaks. Nevertheless, further analysis of the data obtained here may be warranted: As shown in Fig. S11, the SoH extracted using the discharge dε/dV peak position is linearly correlated with that obtained using discharge capacity. This linear dependence suggests that the features extracted from the decoupled strain can further estimate the cell's internal condition.

Recognizing that a non-invasive, non-electrochemical observable parameter (i.e., strain vis-à-vis cell volume change) has the ability to quantitatively track a cell's internal changes over time, the relative evolution of the predominant dε/dV peaks during charge and discharge was explored. In particular, quantitative assessment of the symmetry of the cell's expansion and contraction dε/dV peaks (Figs. 6c and 6d, peaks "a‴" and "b‴") was rationalized as the basis for estimating the cell's overpotential, likely dominated by the internal resistance increase associated with solid electrolyte interphase thickening. Figure 8a shows that after 70 cycles, the primary charge and discharge dε/dV peaks (Peaks "a‴" and "b‴" in Figs. 6c and 6d, respectively) shift positively and negatively in a symmetric fashion, respectively, indicating a continuous rise in electrochemical polarization until the cell's end of life. In this regard, dividing the strain peak potential gap (ΔV_ε) by the applied current (I_{app}) will contain, at least in part, information regarding the changing internal resistance of the cell. As shown by Fig. 8b, the defined constant ($\Delta V_\varepsilon/I_{app}$) declines during the initial 70 cycles while exhibiting a relatively linear increase between the 70th and the 530th cycle, implying that the cell output is limited by sluggish kinetics after 70 cycles. While this evidence is encouraging but inconclusive, further support is obtained from the cycling data. In particular, the evolution trend of $\Delta V_\varepsilon/I_{app}$ is generally consistent with that of the internal resistance (($\Delta V_1 + \Delta V_2$)/ I_{app}) calculated using the total potential recovered during the post-discharge rest, as shown by the inset of Fig. 8b, confirming that the position of the strain differential peaks follows the electrochemical degradation of the cell. Here, the trend of the internal resistance evolution over the cycling span is shown to be governed by that of the ohmic resistance ($\Delta V_1/ I_{app}$) component rather than the charge-transfer and diffusion resistance. Extending the ISA to the graphite-anode chemistry of cell G1 is shared in Supplementary Information (Figs. S12 and S13).

Turning to ISA analysis of the anomalous G2 cell, interesting insights can be gathered preliminarily, as presented in Fig. S14. Herein, discrete peak intensities are individually tracked during charge and discharge clearly demonstrates the spontaneous strain inflation which served as an early warning signal comes only from the peak "b" during charge, corresponding to complications associated with reaching the fully-lithiated state of the graphite anode. However, while this link is interesting, we should not speculate further on the pathology of the spontaneous degradation in this cell.

Collectively, the strain data decoupled from the SMF-POF optical sensing results showcased the strong consistency between the electrochemical and mechanical features for both the graphite- and SiO_x/C-anode LCO-cathode cells over long-term cycling. Therefore, the features extracted from the decoupled strain measured at the package level can effectively characterize cell degradation during cycle aging, enabling reliable on-site health assessment and possibly identifying an abnormal cell within a safe time margin. In addition, the strain data externally obtained by the FBG sensors provide additional health indexes as input for data-driven methods, which explain the internal degradation of the battery, not directly based on the prior knowledge of aging mechanisms, but the evolution trajectory of health-related parameters.
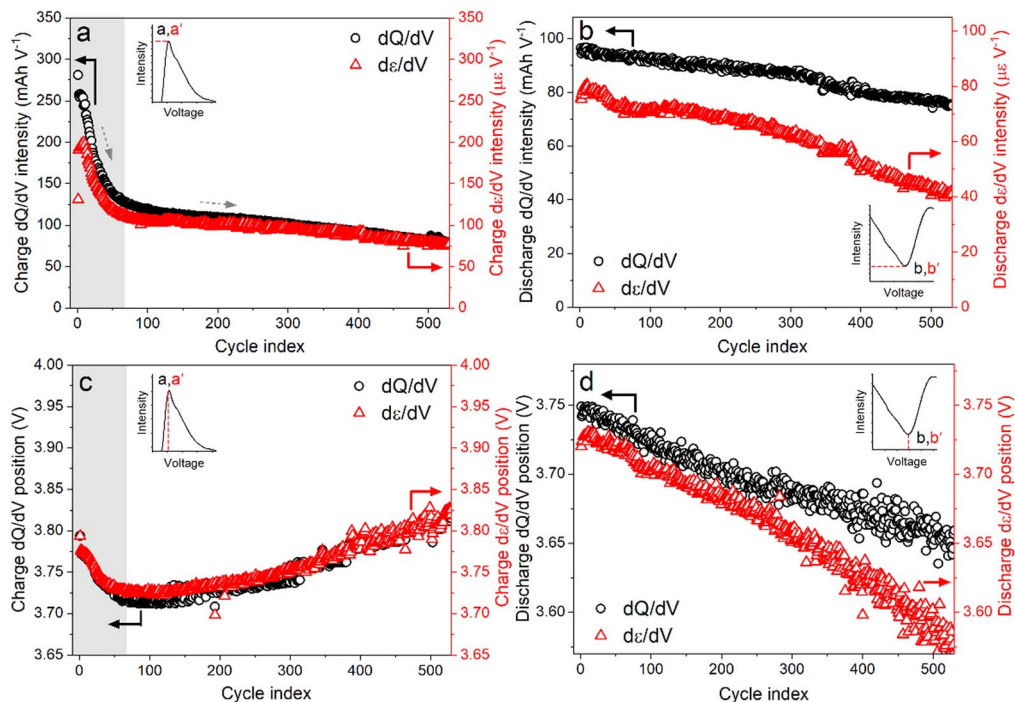
Figure 7. Cell SC: Variation of dQ/dV and dε/dV peak intensity (a), (b) and position (c), (d) during charge and discharge.
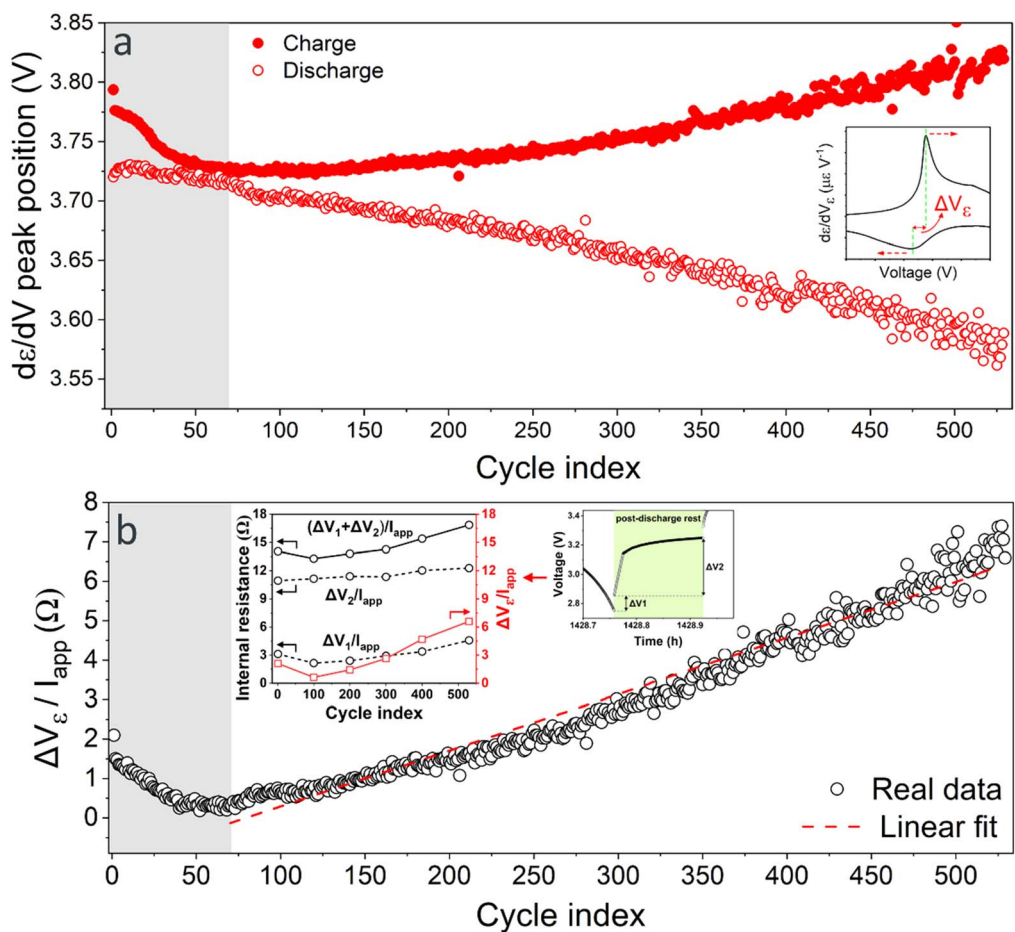

Figure 8. (a) Evolution of the main dε/dV peaks during charge and discharge in cell SC. (b) Variation of internal resistance calculated using the applied current and the overpotential values in (a). The inset of Fig. 8b represents the evolution of the internal resistance (obtained using the post-discharge rest data) of the cell SC versus the $\Delta V_{\varepsilon}/I_{app}$ constant extracted from Fig. 8a data.

Conclusion

Polymer- and silica-based FBG sensors were successfully utilized for operando monitoring of temperature and strain at the package level for commercial Li-ion button cells. The obtained results demonstrated the durability of decoded temperature and strain externally captured by the sensors for over 500 cycles, where a nearly linear correlation was found between the SoH obtained by capacity value and that calculated using strain amplitude.

The strain amplitude trajectory also provided an early indication of abnormal behavior in what would later be revealed as a faulty cell, with mechanically based indicators arising around 200 h before the sudden and significant drop in cell capacity. Although this cell was a single anomaly, the overarching link between cells failing their electrochemical yield criteria, while also exhibiting significant mechanical abnormalities, appears to be strongly correlative thus far. If this relation indeed holds true at the production scale, then it becomes foreseeable that high fidelity strain measurements might be utilized, in part, to assist in detecting abnormal or faulty cell behavior. Collectively, this may help pave the way for further utilization of batteries below the commonly accepted 80% capacity retention and well into a 2nd life scenario.

Utilization of second-order data, such as incremental strain analysis, yields a clear consistency between the evolutions of dQ/dV and dε/dV peak intensities and positions in graphite-anode and SiO$_x$-anode cells over 500 cycles. Although techniques are chemistry-specific, our work shows that symmetric movements of dε/dV may allow for partial determination of well-established health indicators (e.g., internal resistance), which can be extracted from the secondary strain data to improve the accuracy of the cell state estimations. Looking forward, even with precise and accurate real-time measurements of cell volume, further consideration must be given to the dimensionality of cell mechanical information carried by the sensors, as this should prove more valuable than the simple scalar reduction employed here. Thus, approaches using more sophisticated data-driven methods are likely essential to maximizing the value of the information gathered. Nevertheless, these results support the prospects for improved battery safety and reliability through the use of fiber-optic sensors, serving as a step forward on the path towards building better batteries.

ORCID

Sasan Ghashghaie https://orcid.org/0000-0003-3272-4057
Julien Bonefacino https://orcid.org/0000-0001-5147-9873
Steven T. Boles https://orcid.org/0000-0003-1422-5529

References

1. Y. Chen et al., *J. Energy Chem.*, **59**, 83 (2021).
2. B. Xu, J. Lee, D. Kwon, L. Kong, and M. Pecht, *Renew. Sustain. Energy Rev.*, **150**, 111437 (2021).
3. Y. Qiu and F. Jiang, *Int. J. Heat Mass Transf.*, **184**, 122288 (2022).
4. J. Huang et al., *Nat. Energy*, **5**, 674 (2020).
5. S. Yang et al., *J. Clean. Prod.*, **314**, 128015 (2021).
6. K. Mc Carthy, H. Gullapalli, K. M. Ryan, and T. Kennedy, *J. Energy Storage*, **50**, 104608 (2022).
7. X. Li, C. Yuan, X. Li, and Z. Wang, *Energy*, **190**, 116467 (2020).
8. C. Gervillié-Mouravieff et al., *Nat. Energy*, **7**, 1157–1169 (2022).
9. S. Zhu et al., *J. Power Sources*, **516**, 230669 (2021).
10. K. M. Alcock et al., *Sensors*, **23**, 4306 (2023).
11. M. Metzger, B. Strehle, S. Solchenbach, and H. A. Gasteiger, *J. Electrochem. Soc.*, **163**, A798 (2016).
12. S. Lyu et al., *J. Energy Chem.*, **72**, 14 (2022).
13. A. J. Louli, J. Li, S. Trussler, C. R. Fell, and J. R. Dahn, *J. Electrochem. Soc.*, **164**, A2689 (2017).
14. B. Bitzer and A. Gruhle, *J. Power Sources*, **262**, 297 (2014).
15. Y. Li et al., *Adv. Sci.*, **9**, 2203247 (2022).
16. Y. Zeng et al., *Nat. Commun.*, **14**, 8203 (2023).
17. S. Zhu et al., *J. Energy Storage*, **42**, 103049 (2021).
18. I. I. Bezsonov, G. H. Waller, J. Ko, and S. P. V. Nadimpalli, *J. Power Sources*, **592**, 233915 (2024).
19. P. Daubinger, F. Ebert, S. Hartmann, and G. A. Giffin, *J. Power Sources*, **488**, 229457 (2021).
20. P. Ladpli, F. Kopsaftopoulos, and F.-K. Chang, *J. Power Sources*, **384**, 342 (2018).
21. A. Jnawali et al., *J. Power Sources*, **527**, 231150 (2022).
22. Z. Simunovic et al., *J. Electrochem. Soc.*, **170**, 120532 (2023).
23. C.-Y. Lee, W.-Y. Fan, and W.-J. Hsieh, *Sensors*, **10**, 6395 (2010).
24. N. A. David, P. M. Wild, J. Hu, and N. Djilali, *J. Power Sources*, **192**, 376 (2009).
25. G. Han et al., *Renew. Sustain. Energy Rev.*, **150**, 111514 (2021).
26. J. Huang, S. T. Boles, and J.-M. Tarascon, *Nat. Sustain.*, **5**, 194 (2022).
27. G. Yang, C. Leitão, Y. Li, J. Pinto, and X. Jiang, *Measurement*, **46**, 3166 (2013).
28. M. Nascimento, M. S. Ferreira, and J. L. Pinto, *Measurement*, **111**, 260 (2017).
29. L. Albero Blanquer et al., *Nat. Commun.*, **13**, 1153 (2022).
30. C.-J. Bae, A. Manandhar, P. Kiesel, and A. Raghavan, *Energy Technol.*, **4**, 851 (2016).
31. L. W. Sommer et al., *J. Electrochem. Soc.*, **162**, A2664 (2015).
32. M. Nascimento, M. S. Ferreira, and J. L. Pinto, *Batteries*, **4** (2018).
33. J. Bonefacino et al., *J. Electrochem. Soc.*, **169**, 100508 (2022).
34. J. Bonefacino et al., *Light: Sci. Appl.*, **7**, 17161 (2018).
35. X. Cheng, D. S. Gunawardena, C.-F. J. Pun, J. Bonefacino, and H.-Y. Tam, *Opt. Express*, **28**, 33573 (2020).
36. J. He, L. Ding, J. Cai, W. Zhu, and J. Dai, *Results Phys.*, **14**, 102456 (2019).
37. R. Koerver et al., *Energy Environ. Sci.*, **11**, 2142 (2018).
38. J. N. Reimers and J. R. Dahn, *J. Electrochem. Soc.*, **139**, 2091 (1992).
39. K. Pan, F. Zou, M. Canova, Y. Zhu, and J.-H. Kim, *J. Power Sources*, **413**, 20 (2019).
40. T. J. Embleton et al., *Small*, **19**, 2206576 (2023).
41. M. Armand et al., *J. Power Sources*, **479**, 228708 (2020).
42. C. Heubner, M. Schneider, and A. Michaelis, *J. Power Sources*, **307**, 199 (2016).
43. J. Huang et al., *J. Electrochem. Soc.*, **170**, 090510 (2023).
44. J. Huang, C. Delacourt, P. Desai, and J.-M. Tarascon, *J. Electrochem. Soc.*, **171**, 30516 (2024).
45. L. Spitthoff, M. S. Wahl, P. J. S. Vie, and O. S. Burheim, *J. Power Sources*, **577**, 233149 (2023).
46. S. Jenu, A. Hentunen, J. Haavisto, and M. Pihlatie, *J. Energy Storage*, **46**, 103855 (2022).
47. H. Hamed et al., *Batteries & Supercaps*, **6**, e202300140 (2023).
48. H. Li et al., *Small*, **17**, 2102641 (2021).
49. H. Zhou et al., *Colloids Surfaces A Physicochem. Eng. Asp.*, **648**, 129386 (2022).
50. S. Schweidler et al., *J. Phys. Chem. C*, **122**, 8829 (2018).
51. Z. Wang et al., *J. Electroanal. Chem.*, **851**, 113411 (2019).
52. S. Li, S. Tsutsumi, S. Shironita, and M. Umeda, *Electrochemistry*, **90** (2022).
53. T. Kalogiannis et al., *ECS Trans.*, **77**, 403 (2017).